Energy 273 (2023) 127230

Contents lists available at ScienceDirect

Energy

journal homepage: www.elsevier.com/locate/energy

Schlieren analysis of non-MILD distributed combustion in a mixture temperature-controlled burner

Viktor Józsa [a,*], Milan Malý [b], Dániel Füzesi [a], Erika Rácz [a], Réka Anna Kardos [a], Jan Jedelský [b]

[a] Department of Energy Engineering, Faculty of Mechanical Engineering, Budapest University of Technology and Economics, Műegyetem rkp. 3., H-1111, Budapest, Hungary
[b] Faculty of Mechanical Engineering, Brno University of Technology, Technicka 2896/2, 616 69, Brno, Czech Republic

ARTICLE INFO

Handling Editor: Wojciech Stanek

Keywords:
Turbulent
Burner
Swirl
Combustion
Schlieren
Distributed

ABSTRACT

It was recently demonstrated that distributed combustion is accessible outside the MILD combustion regime without needing inner or outer flue gas recirculation. The Mixture-Temperature Controlled combustion concept, which made it possible, offers excellent flame stability besides ultra-low emission. This concept is investigated presently to reveal the qualitative characteristics of the cold discharging mixture jet from the burner and its ignition. The Schlieren technique with a high-speed camera is the most suitable approach for this purpose, revealing the line-of-sight density gradients. Nine cases were evaluated, utilizing natural gas and diesel fuel, various equivalence ratios, and atomizing pressures. V-shaped flames were used as a baseline for comparing distributed combustion to it via direct images and velocity field using the PIVlab Matlab application. The results confirm the previous hypothesis that distributed combustion features a cold fuel-air mixture at the burner discharge that ignites downstream. The excellent flame stability comes from the fishbone-tiled coherent structures with significant random features, resulting in no characteristic frequency related to the flame. All these results comply with the previous findings by chemiluminescence emission and acoustic signal of distributed combustion, which techniques cannot be used to investigate the flame structure, unlike Schlieren imaging.

1. Introduction

Photovoltaic and wind turbine systems provide intermittent renewable energy that needs balancing to maintain grid stability. For this purpose, gas turbines are ideal solutions as they can be quickly ramped up [1] and excellently complement fuel cells and power-to-gas systems [2]. Commercial aviation is expected to rely exclusively on gas turbines powered by hydrocarbon fuels in the upcoming decades, using a continuously increasing share of sustainable aviation fuel [3]. Consequently, advancements in gas turbine combustion are highly desired for cleaner operation since fossil fuels are interchangeable with renewables if the key physicochemical properties match [4]. The operational criteria are wide, reliable, ultra-low emissions [5], and stable operation without thermoacoustic problems [6].

Advancement in gas turbine combustion is governed by national and international regulations [7], new frontiers in control systems, and, most importantly, the understanding of combustion and the associated phenomena [8]. The most critical regulated pollutant today is NO_X, which is a primary focus in combustion system development [9], and if it cannot be avoided, aftertreatment is necessary [10]. Since gas turbines need to feature quick starting capacity and a high turndown ratio, older concepts, such as rich burn-quick quench-lean burn, are still in use due to their simplicity and good combustion stability [11]. Ultra-low emissions can be achieved via distributed combustion, which is generally associated with moderate or intense low-oxygen dilution (MILD) combustion [12]. The challenges of implementing this concept into gas turbines are summarized by Xing et al. [13], including the required recirculation rate and temperature criteria. It was demonstrated recently that distributed combustion could be achieved without oxygen dilution using the Mixture-Temperature Controlled (MTC) combustion concept [14]. The need for excluding external flue gas recirculation is a question of system design, while special combustion chambers may maintain significant internal recirculation to have a highly diluted reaction zone [15], avoiding combustion air dilution by flue gas or inert gas. Such combustion chambers operate with very low chemiluminescent emission [16], similar to MTC combustion [14]. However, MTC combustion is free from external and internal recirculation while offering ultra-low NO_X emission [17]. Consequently, MTC combustion should be compared to traditional swirl burners, which operate with V-shaped

* Corresponding author.
E-mail address: jozsa@energia.bme.hu (V. Józsa).

https://doi.org/10.1016/j.energy.2023.127230
Received 11 August 2022; Received in revised form 12 January 2023; Accepted 15 March 2023
Available online 16 March 2023

Nomenclature

Physical quantity, Description, Unit

d_{mt}	diameter of the mixing tube, mm
h	shear rate, 1/s
I	intensity, count
m	mass flow rate, kg/h
p_g	atomizing gauge pressure, bar
Re	Reynolds number, –
S	swirl number, –
u	horizontal velocity component, m/s
v	vertical velocity component, m/s
w	velocity magnitude, m/s
υ	kinematic viscosity, m^2/s

Abbreviations

d	distributed flame
D	diesel fuel (EN590:2017 standard)
IRZ	internal recirculation zone
NG	natural gas (MSZ 1648:2000 standard)
ORZ	outer recirculation zone
PIV	Particle Image Velocimetry
s	straight flame
v	V-shaped flame

Subscripts

0	instantaneous value
b	bulk
mean	mean value
RMS	root mean square value

flames since they have similar fuel and combustion air inlet conditions. The NO_X advantage of MTC combustion is more than 50% over V-shaped flames, while neither CO nor unburnt hydrocarbon emission is compromised [14]. Moreover, distributed flames show a very low susceptibility to thermoacoustic oscillations, proven recently by combined microphone and photomultiplier tube measurements [18]. This is a critical advantage over V-shaped flames since thermoacoustic instabilities principally bound its lean and safe operation for low NO_X emission.

Schlieren imaging is an excellent tool to visualize supersonic flows [19,20], fires [21], and flame propagation [22] since this technique reveals density gradients through light deflection via the variation of the refractive index. Its use ranges from flame speed measurement [23], non-premixed and premixed laminar flames [24], to fully turbulent, practical flames [25]. Schlieren imaging is especially valuable in evaluating flame structures and the corresponding flow transition from laminar to turbulent [26,27] and resolving flame instability problems [28]. Since the burner discharge in MTC combustion features only a cold mixture without ignition, the resulting flame is classified as lifted. The detailed structures of both attached and lifted flames with the Schlieren technique were analyzed by Owaki and Umemura [29]. Wang et al. [30] presented that stable flames show no characteristic frequency peaks in the Schlieren images by dynamic mode decomposition unless they are excited. Consequently, temporal evaluation of the data should be favored over spectral analysis.

Based on the above research papers, the superiority of the Schlieren technique over other optical measurement methods for this particular investigation is the following. An imaging technique is essential to simultaneously measure the entire region of interest, while invasive techniques significantly bias the results. The 10 kHz sampling frequency is either available with low laser intensity per impulse [31] or limited by the number of consequent images per burst [32], which is needed for the present analysis, as it will be detailed later in Section 2. Low laser intensity increases uncertainty in detecting the particles by Particle Image Velocimetry, PIV. This issue is solved by burst recording, which falls behind when statistical properties are important due to the lack of a statistically significant number of recorded images. The line-of-sight measurement means a qualitative advantage in flame front detection compared to laser sheet-based techniques, while their downside is the integration across the control volume. Evaluating the discharging cold mixture from the burner is also an important part of the investigation, which cannot be detected by, e.g., fluorescence techniques used for reaction zone analysis. The boundary of the cold jet is sharp on the Schlieren images due to the high density gradient, while it is less clear on a PIV image, especially in the downstream region.

This experimental study presents the Schlieren imaging analysis of a distributed flame since this technique is the most suitable for revealing spatial ignition characteristics for the following reason. Ignition is accompanied by heat release, resulting in a rapid temperature increase and high density gradients. The achieved distributed combustion is well outside the MILD combustion regime, i.e., there was no external or notable internal flue gas recirculation, which ultimately results in a low-oxygen dilution condition. Also, no existing theory predicts distributed combustion within the discussed operational regime. This work is the first to comprehensively present the flame characteristics by the Schlieren imaging technique of non-MILD distributed combustion. Instantaneous, mean, and root means square intensity values velocity fields were evaluated, including their mean and temporal evolution. Since the used swirl burner can also operate in the well-known straight and V-shaped flame modes, these flames served as baselines to discuss distributed combustion and highlight the differences. The hypothesis made earlier and experimentally not proven is that distributed combustion is made possible by the cold fuel-air mixture that delays ignition, allowing more time for mixing, resulting in a highly homogeneous reaction zone.

2. Materials and methods

The present section introduces the experimental test rig, details the combustion conditions, and highlights the investigated cases and key operational parameters. The second subsection details the evaluation methods, extensively relying on the PIVlab application [33] for Matlab, and includes a flowchart detailing all the presented statistical and velocity field analysis, starting from raw data.

2.1. Experimental setup

The experimental setup is presented in Fig. 1. The dimensions of the burner head, shown in a cross-section, are detailed in the following text due to the more than one magnitude range. The inner diameter of the central fuel pipe (brown) is 1.2 mm, while the annular atomizing air nozzle (blue) has a 1.5 mm inner and 2.2 mm outer diameter. The natural gas was introduced via 12 nozzles with a 1.3 mm diameter (yellow), evenly distributed along a 12.5 mm diameter circle. The 45° swirl vane had eight blades, and its hub and tip dimensions were 21 mm and 40 mm, respectively. The uncertainty of the combustion air temperature was 2.2 °C, while that of the pressure transmitter was 1 kPa; all instruments were calibrated by us, focusing on the measurement range. The test conditions are summarized in Table 1 with the same parameter matrix as in Ref. [14], i.e., using a uniform thermal power and varying atomizing gauge pressure, p_g, and equivalence ratio, φ, which was determined from the flue gas O_2 concentration that features 0.2 V/V% uncertainty. Hence, the accompanying uncertainty of $\varphi = (21\text{-}O_2)/21$ was <1.7%. In addition to standard diesel fuel (D, EN:590:2017),

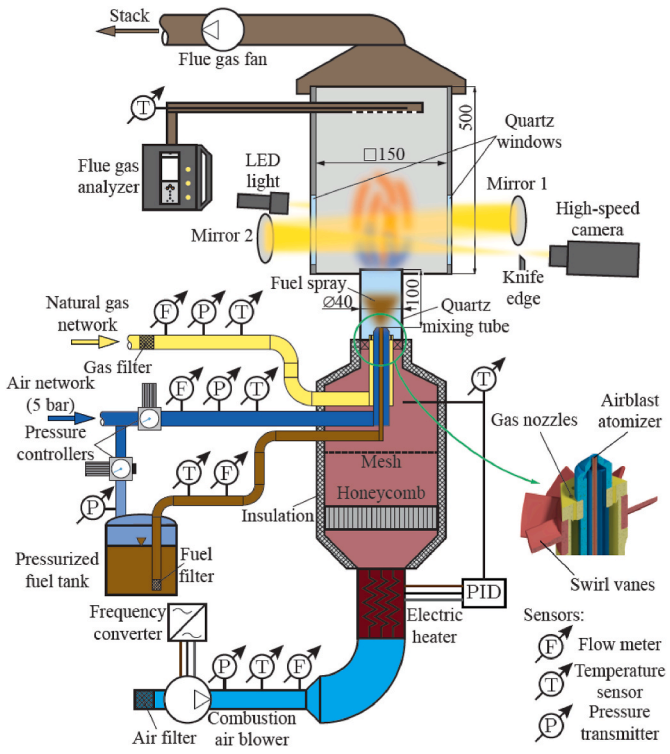

Fig. 1. The test rig with the Schlieren setup.

Table 1
Test conditions.

Parameter	Value
Thermal power	13.3 kW
Combustion air temperature	200 °C
p_g	0–0.9 bar
Φ	0.57–0.76
Fuel	NG, D

standard natural gas (NG, MSZ 1648:2000) combustion was also performed as a reference since its characteristics are well-known in the literature [34]. Combustion modes, flame images, and pollutant emission data were discussed earlier [14]. The Schlieren setup provided excellent quality images since no burning droplet cloud was observed, which would otherwise require an advanced optical setup [35]. A Fujifilm HS10 commercial digital camera was used to record photos at characteristic flame shapes using 1/30 s shutter speed, f/4, and ISO–400 settings.

Two mirrors with a focal length of 750 mm and a diameter of 150 mm were selected for Schlieren measurement in the Z arrangement. A FASTCAM SA-Z type 2100 K-*M*-16GB (Photron, Japan) high-speed camera was used at 10 kHz for image acquisition with 1024 × 1024 pixel resolution, which corresponds to 86 × 86 mm physical size. This framerate allows sufficient tracking of the flame temporal evolution for the 1 MPixel image resolution. The camera was calibrated several times during the measurement campaign due to, e.g., slow heating of the camera sensor, leading to different dark current values. Therefore, there is no basis for quantitative comparison for different setups; only image sets within a single case can be compared. Since the Schlieren technique is already a qualitative evaluation tool, this fact does not imply any notable bias. Flame illumination was provided by an HPLS-36DD18B (Lightspeed Technologies, USA) pulsed LED light source.

The evaluated test cases are summarized in Table 2. Nine were highlighted instead of discussing all the 20 measured cases since the others were similar. The only difference between the setup of [14] and the present measurements is that the mixing tube lip was 25 mm above the base plate of the combustion chamber instead of 15 mm to see the mixing tube lip and the discharging mixture in the Schlieren images. It also led to a slightly earlier transition to distributed combustion, d, in terms of atomizing pressure. The observed flame shapes for all conditions are shown in Fig. 2. Cases 1 and 2 show V-shaped, v, and straight, s, flame of natural gas combustion. Case 3 was unique since the observed flame shape was altered between d, v, and s through the recording interval. The identification of various flame shapes is detailed in Subsection 3.1. Since this was recognized during the measurement; consequently, 3038 frames were saved instead of the regular 2000. Even though a higher number of images were also acquired during the preliminary tests with all flame shapes, the extra data contained no more information. 1–200 showed distributed combustion, then the next 700 frames (0.07 s) presented a transition between d and v. Stable V-shaped flame lasted for 300 frames, then after 400 frames, s was finally stabilized. Note that this tristable state randomly featured all three flame shapes, which is excellent for fundamental analysis and unwanted in practical applications. Even though the number of frames in Case 3 is much lower than in the other cases, the advantage of evaluating its operation is the guaranteed similar conditions in both the measurement and camera recording, providing an excellent opportunity for unbiased comparison of various flame shapes.

Table 2 also contains the Reynolds number, Re, calculated from the conditions of Table 1 at the burner outlet as:

p_g [bar]	Φ 0.57	0.67	0.76	0.86
0.9	d	d*	d	d
0.75	d*	d*	d*	s
0.6	d	d*	d-s	s
0.45	d	d*	s-d	s
0.3	v-d-s*	v	s-d	s

Fig. 2. Flame shapes at each measurement point. Light blue (d): distributed combustion; brown (v): V-shaped flame; orange (s): straight flame; light green (t): transitory flame, including the abbreviation of all observed flames, following the order of their dominance. * represents the presented cases, included in Table 2.

Table 2
Evaluated test cases.

Case N°	Fuel	φ [−]	p_g [bar]	Shape	Re [−]	$\dot{m}_f$ [kg/h]	$\dot{m}_{aa}$ [kg/h]	$\dot{m}_{ca}$ [kg/h]	S [−]
1	NG	0.67	–	v	7766	0.96	0	24.4	0.78
2	NG	0.67	0.3	s	8435	0.96	1.73	22.6	0.29
3	D	0.67	0.3	d, v, s	9102	1.12	1.73	22.3	0.34
4	D	0.57	0.75	d	10,928	1.12	2.72	25.4	0.25
5	D	0.67	0.75	d	9533	1.12	2.72	21.4	0.2
6	D	0.76	0.75	d	8488	1.12	2.72	18.3	0.16
7	D	0.67	0.45	d	9264	1.12	2.10	22.0	0.27
8	D	0.67	0.6	d	9401	1.12	2.41	21.7	0.23
9	D	0.67	0.9	d	9654	1.12	2.99	21.1	0.17

$$\mathrm{Re} = \frac{w_{\mathrm{b,mean}} \cdot d_{\mathrm{mt}}}{\nu_{\mathrm{mean}}} \quad (1)$$

where $w_{\mathrm{b,mean}}$ is the mean bulk velocity inside the mixing tube, $d_{\mathrm{mt}} = 40$ mm is the inner diameter of the mixing tube, and υ_{mean} is the mean kinematic viscosity, calculated using a simple mixing rule, considering the temperature of the inlet streams. These are presented in the following three columns as the mass flow rates of fuel, $\dot{m}_f$, atomizing air, $\dot{m}_{aa}$, and combustion air, $\dot{m}_{ca}$, respectively. Based on the Re values, it can be concluded that the flow is entirely turbulent. The uncertainty of the diesel fuel volume flow rate was <2.7%, while the density measurement uncertainty was below 1%, assuming normal distribution and a 95% level of significance. The natural gas flow rate was measured by a utility gas flow meter. The gas company provided its lower heating value and composition [36], and the gas density was calculated from its chemical composition. Since the uncertainties are legally regulated, and the actual uncertainty is not disclosed by the gas company, the uncertainty of the gas flow rate was not determined. The uncertainty of the atomizing air mass flow rate varied between 4.2% and 2.3%, based on the flow rate determined by p_g. The combustion air flow rate was calculated from the stoichiometric air of the fuels, φ, and $\dot{m}_{aa}$ that offered lower uncertainty than the used Fuji FWD050D2-A52 ultrasonic air flow meter.

The final estimated quantity is the geometric swirl number, S [37]. The relatively low values are the direct consequence of the significant axial momentum added by the atomizing air jet. Otherwise, if only combustion air is introduced and no atomizing air, $S = 0.78$, as shown in Case 1. This value exceeds $S = 0.6$, often treated as the critical swirl number required for V-shaped flames [37]. Even though Case 3 features $S = 0.34$, which is well below 0.6, a V-shaped flame was partially observed, implying that the momentum transfer between the annular swirling hot combustion air and the cold atomizing jet was not completed by the mixing tube outlet.

The combustion chamber should be above 700 °C to provide a lifted flame, which is classified as unstable since it leads to blowout [38]. In the present case, the outer surface of the combustion chamber wall was measured with a touch probe K-type thermometer in several operating conditions with temperatures between 425 and 430 °C. This is in line with the observations since the inside of the combustion chamber became dark red only for V-shaped flames, which come with a high-temperature zone at the flame tip, while neither straight nor distributed combustion colored the combustion chamber walls red. Another critical observation of [38] is that the startup procedure should rely on flame; flameless combustion is only possible after the initial warm-up period. This was confirmed in our case; distributed combustion was possible only after a few minutes of operation with either NG or D due to the quenching effect of the cold combustion chamber walls.

2.2. Data processing

All the calculations were performed on the raw images containing intensity information at each pixel. After all calculations and image manipulation was complete, the displayed intensity images were adjusted for better visibility using the *imadjust* Matlab function [39], which saturates the top and bottom 3% of the pixels by intensity to improve contrast for better visualization. The entire procedure is shown in Fig. 3, presenting all the processes discussed in this subsection for Case 5 as an example.

Two processing methods were used on the raw intensity, mean calculation, I_{mean}, and root mean square, I_{RMS}. The first images were displayed to show an instantaneous intensity distribution, denoted with I_0. The PIVlab application [33] calculated flow velocities, and their mean, w_{mean}, and RMS, w_{RMS}, were also presented. The application calculates the velocity field from image pairs from the correlation between the two subsequent images, using interrogation windows of three sizes for coarse, medium, and fine velocity field decomposition.

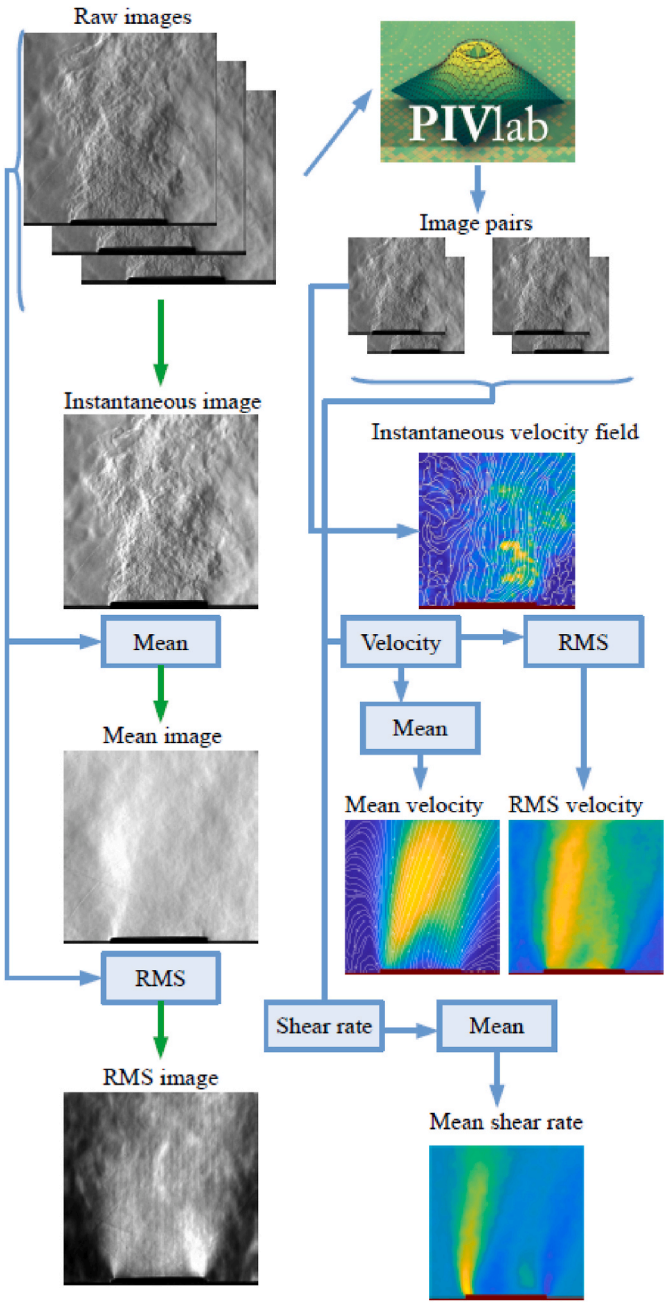

Fig. 3. Data processing algorithm. Green lines mark the use of the *imadjust* Matlab function.

Depending on the setup, the top level varied between 72 and 96 pixels; therefore, the smallest tile sizes were their quarter, i.e., 18–24 pixels. The interrogation area of image pair evaluation was automatically determined using three levels. The shear rate, h, excellently revealed the cold mixture boundaries on the sides, calculated as [40]:

$$h = \frac{\partial v}{\partial x} + \frac{\partial u}{\partial y} \quad (2)$$

where u and v are the velocity components of the x (horizontal) and y (vertical) directions, respectively.

The Schlieren technique reveals the density gradients in line-of-sight. Therefore, the results are respective to the projections of three-dimensional bodies with temporal evolution characterized by high density and hence high temperature gradients. Consequently, the flow field properties are respective to the regions with increased gradients

instead of a cross-sectional plane, like in PIV measurements. Regardless of this condition, the resulting information was highly valuable since it reveals both the evolution and the spatial structure of the heat release of all observed flames. The only notable bias was present during the evaluation of V-shaped flames, where the line-of-sight measurement means that the foreground zone was moving left and the background zone was moving right at the center. This effect has a decreasing relevance towards the periphery due to the cylindrical flame structure and was marginal in the case of both straight and distributed flames. Nevertheless, the horizontal velocity component bias cannot be fully resolved in Schlieren image processing.

The uncertainty estimation of the velocity field was performed based on [41]. It was found that neither the flame shape nor other parameters notably affect the absolute uncertainty. The mean uncertainty was 0.46–0.51 m/s, the standard deviation was 0.18–0.23 m/s, and the maximum value was between 1.11 and 1.21 m/s. These values are similar to ones calculated by commercial PIV software codes for PIV measurements. The only bias is the above-mentioned tangential movement of the tracked fluid packets, which cannot be quantified with the present setup; only a tomographic analysis would resolve this issue [42], which is beyond the capabilities of our lab.

3. Results and discussion

Firstly, this section presents an instantaneous, mean, and RMS image of all cases, arranged into three groups: comparing various flame shapes and the effect of equivalence ratio and atomizing pressure on distributed combustion, which is of primary interest in this paper. The second subsection focuses on the statistical properties of fluid dynamic characteristics of the images using the PIVlab Matlab application. The hot flue gas continuously leaves the combustion chamber; the only inlet is through the burner. Therefore, the revealed features present either an igniting cold fuel-air mixture (V-shaped flames, distributed combustion, and cold fuel-air mixture packets in straight flames) or a hot flame surrounded by the cooler flue gas (straight flames only). Lastly, flame dynamics are presented in two parts. The first one details the evolution of the flame characteristics at highlighted conditions based on a comparison of the raw images using a false-color technique. The second part shows the temporal evolution of the velocity field calculated by PIVlab.

3.1. Direct image evaluation

Fig. 4 shows the anatomy of four flames by combining a color photo, recorded by the Fujifilm commercial camera, and a Schlieren image, recorded by the Photron high-speed camera. The V-shaped reaction zone is visible due to the igniting mixture right downstream of the mixing tube for both NG and D, as shown in Fig. 4a and b. The blue light is emitted by the excited CH radicals, which strongly correlate with the heat release [43]. The cold mixture is also visible at the center in the case of D since both the internal and outer recirculation zones, IRZ and ORZ, respectively, characterizing flames with strong swirl [44], contain relatively low temperature variation in these vortices. Consequently, they are invisible in the Schlieren images. However, the characteristic stems of the V are clearly visible in both the color photos and Schlieren images.

The ignition process along the stems of the V can be tracked due to the accompanying density gradients; the small fluid packets increase in size along them until they reach the temperature of the surrounding flue gas, then they blend into the background. This phenomenon was also observed by Yen et al. [26] and Owaki and Umemura [29]. Mixing air with NG is always quicker than with D since NG is already in the gas phase. In contrast, D has to be atomized into tiny droplets and evaporated in advance, leading to a less homogeneous mixture at the small scales. This is the reason for the visible small fluid packets in Fig. 4b, while Fig. 4a shows more uniform stems of the V in the case of NG. See Supplementary videos 1 and 2 (36–48 s) for the temporal evolution of these flames.

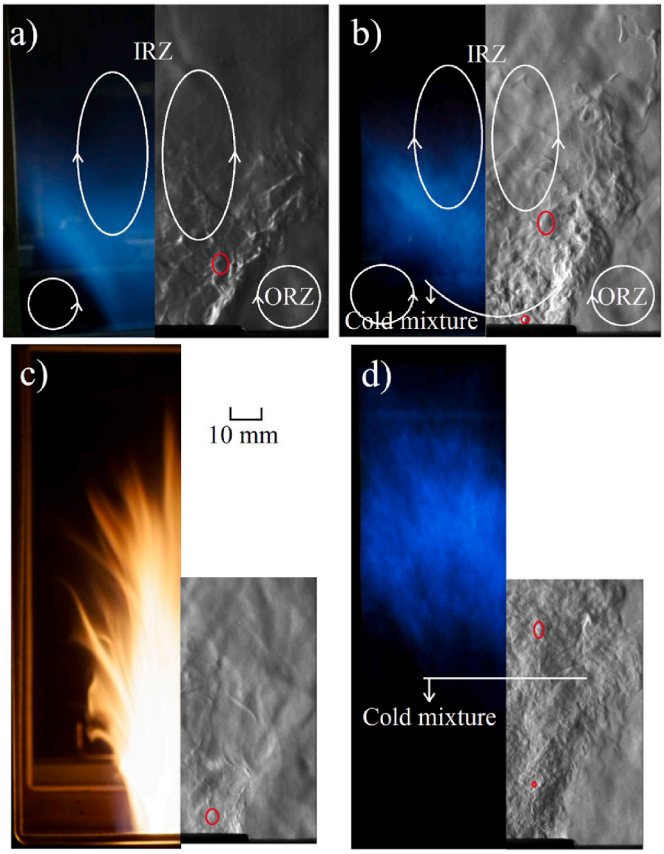

Fig. 4. Schlieren image and a photo of the observed flames: a) Case 1, b) Case 3v, c) Case 3s, and d) Case 9. The sections of the internal and outer recirculation zones are marked with ellipses. The red ellipses show a single vortex. Color intensity was tripled in Case 9 for better visibility. All photos were taken at ISO 400, 1/30 s, and f/4.

The roots of straight flames are located inside the mixing tube. Therefore, the discharging reacting gas is already hot, leading to a significantly lower contrast in the Schlieren image. Here, an entirely yellow flame brush is visible in the regular picture; see Fig. 4c and Supplementary video 2 (1:04–2:01). Since the other flame shapes are dominated by blue color, identifying a straight flame was easily performed by visual observation. There are discharging cold, igniting fluid packets occasionally appearing even in the straight flames with a size in the range of 10 mm, which appear as the dancing of the turbulent flame brush to the human eye. Therefore, the corresponding vortical structures are significantly larger than that of V-shaped and distributed flames since the reacting gas is already hot and partially expanded as ignition occurred well upstream of the combustion chamber inlet. Nevertheless, these vortexes are smaller than such structures in the post-flame zone, indicated by red ellipses in Fig. 4.

Distributed combustion shows a cold discharge in the entire cross-section of the mixing tube, revealing that ignition occurs only inside the combustion chamber downstream of the burner, as shown in Fig. 4d and Supplementary video 3. The first 8 s of Supplementary video 2 also feature distributed combustion. The evolution of fuel-air mixture packets is similar to that of V-shaped D flame, except that they are distributed uniformly and ignite well downstream. The small cold fluid packets with high contrast, see the 'Cold mixture' part of the image, and their fading as ignition occurs, accompanied by a blue flame, were also observed by Wang et al. [30] in a bluff-body-stabilized burner. Based on the photo and the Schlieren images, the reader might think that the distributed combustion here is similar to a lifted flame, also known for

featuring low NO_X emissions. The difference between distributed combustion here and the lifted flame is that the latter maintains the preceding V-shape [45] or features a transition to W [46]. In contrast, distributed combustion showed no characteristic shape and occupied the entire cross-section of the combustion chamber, leading to volumetric heat release rates similar to flameless or MILD combustion [16]. Concluding from the above phenomena, the identification of distributed combustion was facilitated by the following properties. It occupied the entire cross-section of the combustion chamber with a faint blue flame that detached from the burner lip. Also, the combustion noise was reduced by about 8 dB compared to V-shaped flames and 10 dB compared to straight flames [18], which the system operators clearly heard during the measurement. Also, the pollutant emission significantly dropped [14]. Regarding the Schlieren images, the cold discharging mixture has more contrast than the hot flue gas in the hot combustion chamber.

Fig. 5 shows instantaneous, mean, and RMS images of all the observed flame shapes for both fuels. The difference in the flow structure of V-shaped flames of NG and D was already discussed in Fig. 4, detailing the grainy features of the mean and RMS images. The other reason for the grains is that only 300 images were used for Case 3v, while it was 2000 for Case 1, as detailed in Subsection 2.1. The mean and RMS images show the characteristic V since the density gradients and their fluctuation are confined to this region.

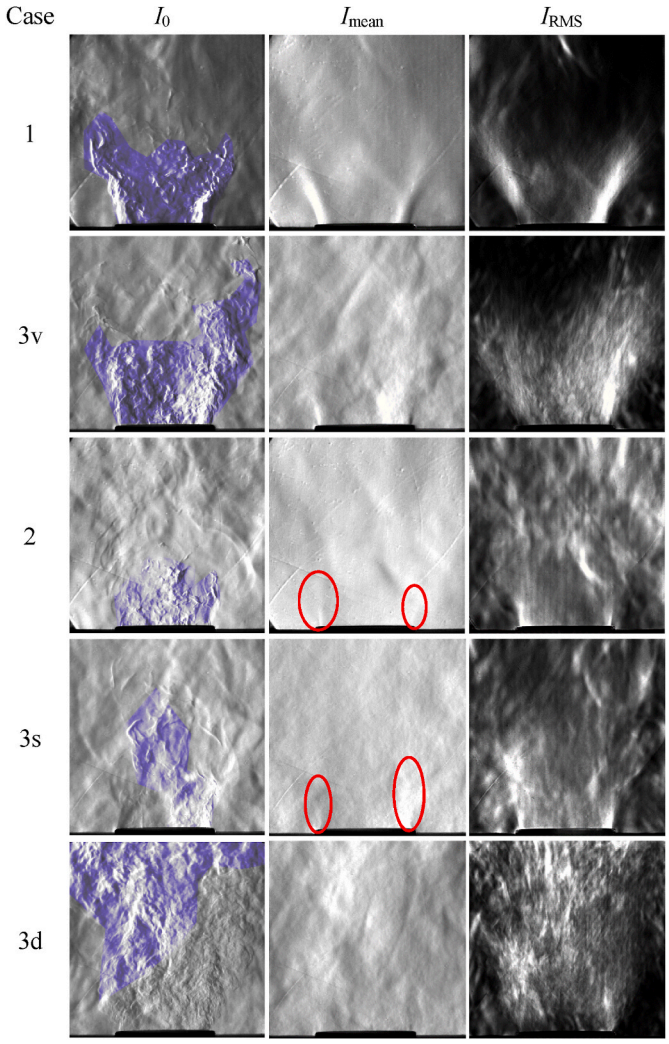

Fig. 5. Instantaneous image, mean, and RMS of the observed flame shapes of the first three cases at $\varphi = 0.67$. Red ellipses on I_{mean} images of straight flames highlight the relatively intense mean gradients, marked by red ellipses.

I_{mean} and I_{RMS} feature 1438 images for Case 3s, and that of Case 2 is 2000, which are comparable. Ignition starts inside the mixing tube for both cases; therefore, the difference in Schlieren images between them is marginal. However, D features a yellow, and NG a blue flame brush since NG requires significantly less residence time for homogeneous mixture formation. Due to the low density gradients, the mean images of straight flames feature only two short vertical zones, showing high gradients downstream of the mixing tube, marked by red ellipses. This location has the highest density gradients, and the discharging reacting gas flows axially. These structures are more emphasized in the I_{RMS} images for both fuels, up to a mixing tube inner diameter size downstream. The occasionally observed igniting cold fuel-air mixture packets disappear quickly, leaving no notable trace in the mean or RMS images. The random noise of Cases 2 and 3v on RMS images are alike.

Distributed combustion is special since its instantaneous shots always show a cold discharging mixture that ignites in the upper part of the combustion chamber, which is marked with a blue patch to emphasize the region of ignition on all images. This was performed manually by checking each image and highlighting the area where the small vortices with sharp edges were significantly enlarged and became blurry. The distinct vortex sizes before and after ignition are presented in Fig. 4, which were used to create the blue patches. Since the vortex sizes were similarly small in the cold and similarly large hot regions, the distinction between the reacting and non-reacting regions was unbiased. The transition from the small fuel-air mixture pockets to combustion occurs over a few centimeters. The mean of 200 images of Case 3 d shows tiny edges right after the mixing tube, while the RMS image reveals a random structure within the main stream. The low number of images inevitably contributes to coarser statistical results, which is compensated in Figs. 6 and 7 by evaluating 2000 frames of distributed combustion.

Fig. 6 shows Cases 4–6, covering three equivalence ratios, 0.57, 0.67, and 0.76, at a uniform atomizing gauge pressure of 0.75 bar. Since the thermal power was also uniform, the increasing equivalence ratio means decreasing bulk flow velocity. Therefore, the majority of the heat release can be seen in Case 6 with the ignition of a mixing tube diameter downstream from the lip, as shown by the blue patches. These features of Cases 4 and 5 are shifted further downstream. The mean images show the blurry edges of the cold discharging jet, while the reacting flow is

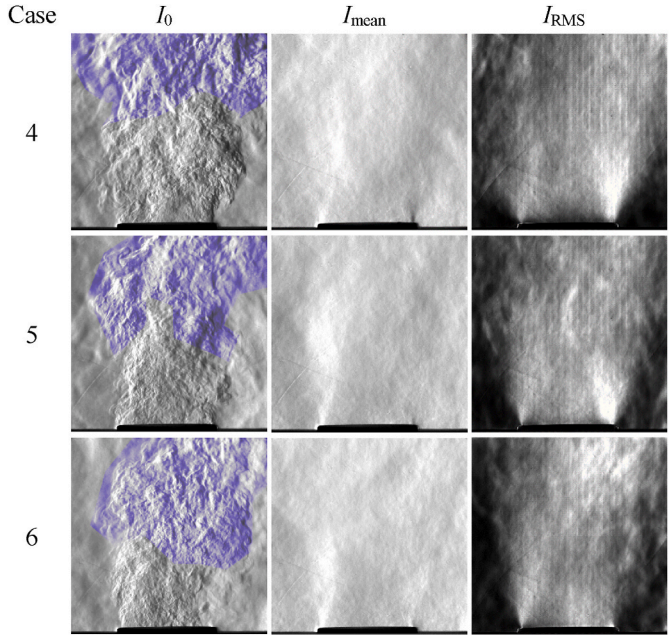

Fig. 6. Instantaneous image, mean, and RMS at $\varphi = 0.57$, 0.67, and 0.76 (top to bottom) and $p_g = 0.75$ bar.

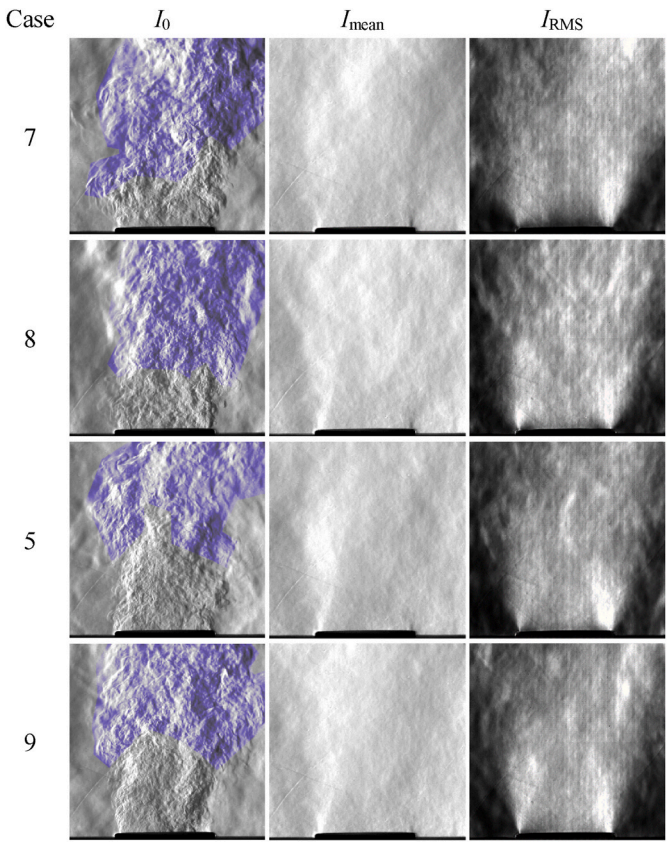

Fig. 7. Instantaneous image, mean, and RMS at $p_g = 0.45$, 0.6, 0.75, and 0.9 bar (top to bottom) and $\varphi = 0.67$.

noisy. The RMS images show that the flame is leaning right due to fluid dynamical asymmetry caused by small imperfections during manufacturing and assembling the burner. Such a phenomenon is common in experimental investigations of in-house developed burners [47]. It was turned out later that this slight asymmetry was particular to the 13.3 kW thermal power; it disappeared at both lower and higher thermal powers. The cold mixture parts are homogeneous, and higher intensities mark the edges. In the reaction zone, notable random fluctuations are present even with the averaging of 2000 frames.

Fig. 7 shows Cases 5 and 7–9 to highlight the effect of p_g in the 0.45–0.9 bar range while keeping the equivalence ratio constant. Due to this latter constraint, the bulk flow velocities are similar, while the spatial distribution differs. The results show ignition occurs downstream with increasing p_g, shown by the blue patches of I_0 images. Due to the fluctuating reaction zone volume of distributed combustion, it is not clearly indicated on the I_{mean} and I_{RMS} images. However, the lower edge of the reaction zone does not show notable axial fluctuation in the long term, as shown in Supplementary video 3. This behavior was observed for all distributed combustion cases. Even though increased shear rate fosters earlier ignition [48], increased p_g also means increased atomizing air flow rate with decreasing atomizing air discharge temperature. The two competing phenomena ultimately increase the ignition delay time, which exponentially decreases with mixture temperature [49]. Lower p_g also features larger mixture packets originating from the lower shear rate.

3.2. Flow field analysis of distributed combustion

Fig. 8 shows the mean and RMS velocities and the shear rate, according to Eq. (2), for Cases 4–6, highlighting the effect of the equivalence ratio on distributed combustion. The mean velocity images with streamlines show clearly that the flame is leaning to the right, which was

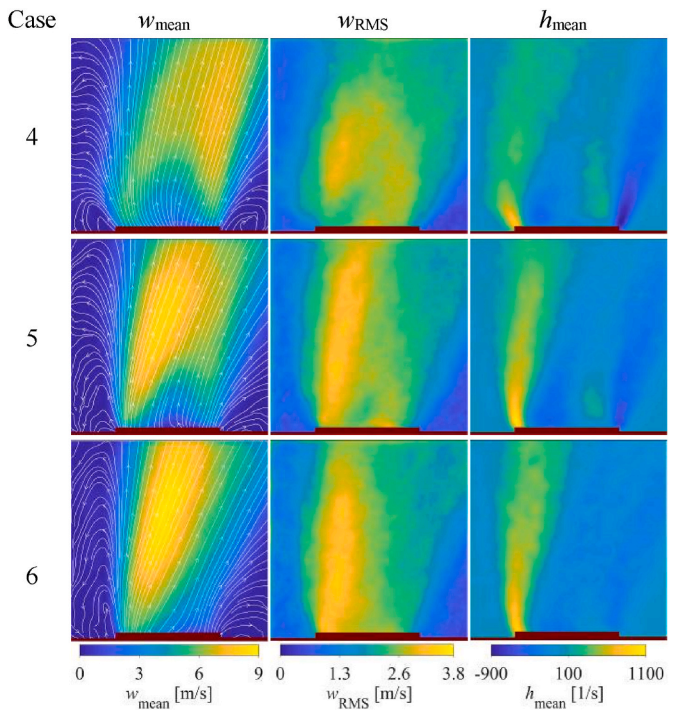

Fig. 8. Mean velocity magnitude, velocity RMS, and mean shear rate at $\varphi = 0.57$, 0.67, and 0.76 (top to bottom) and $p_g = 0.75$ bar.

previously observed in Figs. 6 and 7. Note that recirculation zones were identified outside of the main stream. Since the density gradient is relatively low in these regions, the present paper omits the estimation of the reactant dilution ratio, while a numerical result is discussed in Ref. [17]. φ increases with the case number while the mixture mass flow rate decreases. The effect of the reduced flow rate is not evident on the velocity distributions since ignition occurs earlier with the lower mass flow rates, leading to increased velocities due to the expanding reacting gas. The most diluted mixture resulted in the lowest velocity field fluctuations with a relatively homogeneous distribution. Cases 5 and 6 show the edges of a straight discharging mixture. The mean shear rate highlights the edges of the RMS velocity field, starting from the mixing tube lip. Its intense region lasts longer and disperses for Cases 5 and 6, while the mixing tube discharge is the highlighted region of Case 4 on both sides.

Fig. 9 shows w_{mean}, w_{RMS}, and h_{mean} for Cases 5 and 7–9, similar to Fig. 7. The shared mass flow rate provided more clear trends, i.e., all the presented variables were globally increasing with p_g. The plots of Case 7 show a high similarity to those of Case 4 in Fig. 8. The asymmetry of the flame, discussed in Fig. 6 of Subsection 3.1, is also present in Fig. 9, which is evident on the w_{mean} and w_{RMS} images, while the results of h_{mean} are more symmetric. Therefore, this behavior is not a temporal flame characteristic but is present in the bulk flame properties.

3.3. Flame dynamics

The evolution of the vortical structures of V-shaped flames is well-documented in the literature for natural gas-air [34] and methane-air [50] flames. False-color image pairs of Fig. 10 were separated by 1 ms, i.e., the change over nine frames is presented using the *imshowpair* Matlab function. Green corresponds to features of the original image, which were altered or moved in the second image with characteristics colored magenta. The purpose of false-color illustrations is to show the differences in the temporal evolution of the characteristic features inside the combustion chamber. This representation is often used in many fields, such as Earth observation, to track the seasonal variation of, e.g.,

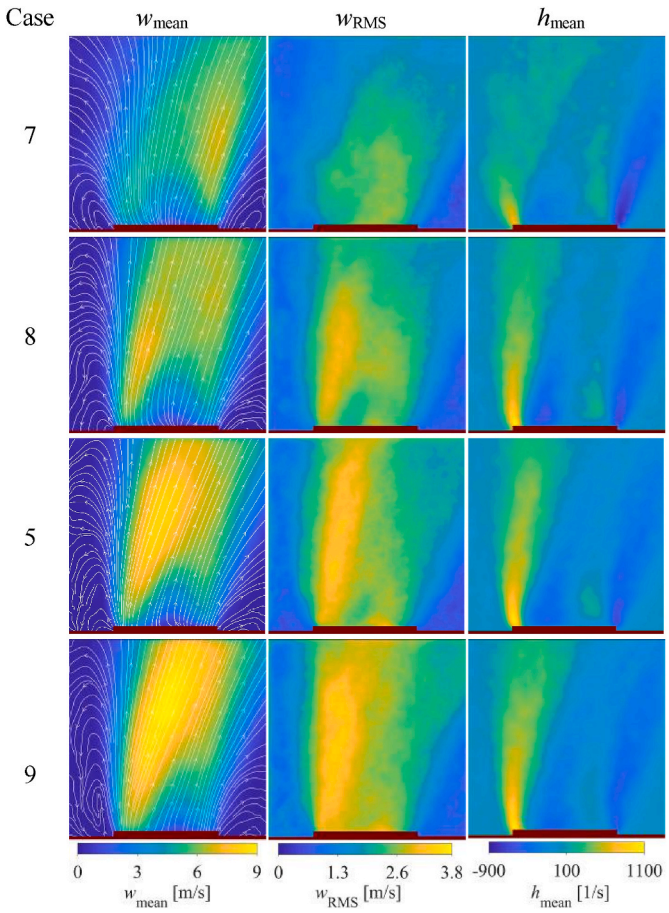

Fig. 9. Mean velocity magnitude, velocity RMS, and mean shear rate at p_g = 0.45, 0.6, 0.75, and 0.9 bar (top to bottom) atomizing pressures and φ = 0.67.

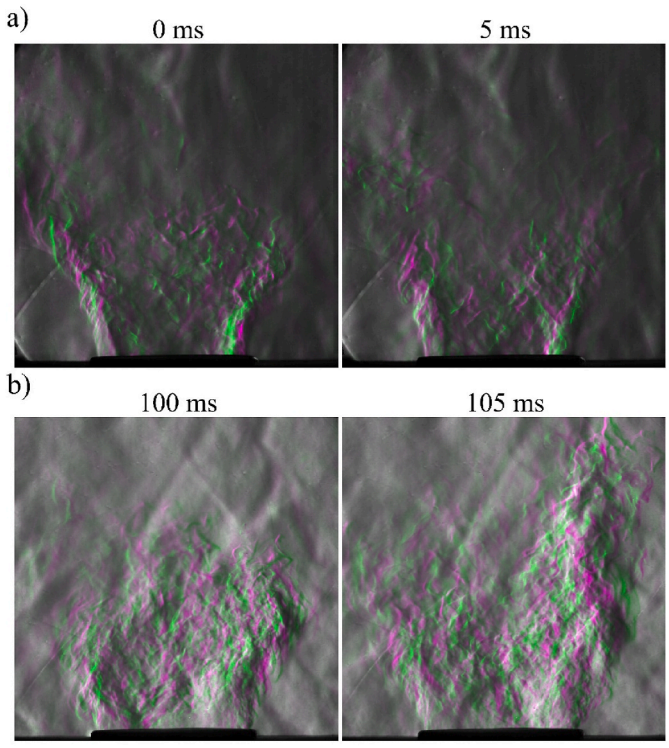

Fig. 10. False-color images of V-shaped flames. a) Case 1 (NG) b) Case 3v (D).

water surfaces [51] to highlight all differences between two images that are not evident to the observer at first look. The revealed moving vortices, i.e., the magenta features, which were previously present as green, of NG are in line with literature data [50,52]. Only two image comparisons were presented for each setup to allow a better visual experience, separated by 5 ms, i.e., the first frame was compared with the tenth, resulting in one false color image, and the 50th was compared with the 60th, providing the second image. The same holds for the following false-color images. If the recording time difference between images is too low, the difference is insufficient, while excessive dime delay comes with too many changes. The 1 ms showed the best result by checking all possibilities from 0.1 ms to 50 ms.

Even though line-of-sight measurement was performed, the stems of the V encompass the most significant changes, marked by the concentrated green and magenta color patches here. The region between the left and right stems of the V features the movement of small vortices on the surface of the conical reaction zone. The difference between NG and D in Fig. 10 is that the random movement of the small vortices originates from the less homogeneous fuel-air mixture, resulting from the evaporating fuel droplets. Their vapor can mix only later with the combustion air. Globally, the growing stems of the V are observable, a temporal feature of this particular D flame. Even though the magenta and green zones are not as concentrated here as in the case of the NG flame, they are similar.

False-color images of two distributed combustion cases at p_g = 0.75 bar are shown in Fig. 11. The contrast of the images at φ = 0.57 was more significant than that at φ = 0.76. The microstructures are random, also presented in Fig. 10, while a few fishbone tile-shaped global structures were revealed in both cases, as shown by red lines on the 0 ms images of both cases. Since these highlight coherent structures with continuous ignition due to their orientation, they feature no characteristic frequency as their heat release is elongated in time, as presented in a preceding work for diesel-biodiesel combustion in this MTC burner [18]. This finding is critical in flame blowout stability since if there is no

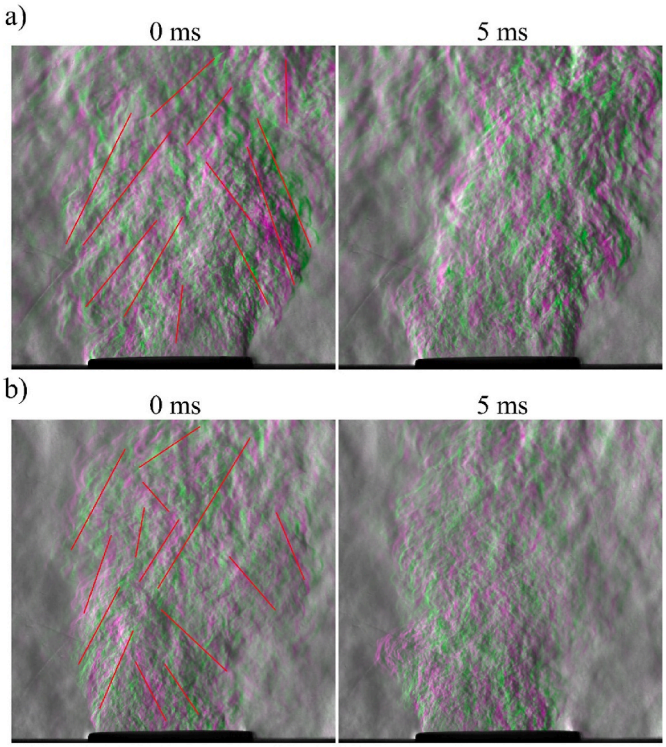

Fig. 11. False-color images of distributed flames at p_g = 0.75 bar. a) Case 4 (φ = 0.57) b) Case 6 (φ = 0.76). Red lines on the 0 ms images show some fishbone tile-shaped coherent structures.

apparent characteristic frequency of the flame and the ignition is continuous, a flame blowout can only be reached close to the theoretical equivalence ratio limit of the fuel. This finding was supported by low CO emissions, discussed in earlier works [14,18]. Moreover, the green and magenta markings are more evenly distributed along the discharging mixture jet. The jet is leaning to the right in the second image of Fig. 11a, which underwent a small oscillation due to the quasi-steady nature of turbulent flames.

Fig. 12 shows distributed combustion at $\varphi = 0.67$ at two atomizing pressures. As expected, the microstructures are larger in the case of $p_g = 0.45$ bar since $p_g = 0.9$ bar creates more intense shear and finer vortices. The fishbone tile-shaped coherent structures are also present in Fig. 12, sharing the key characteristics with Fig. 11. This is the principal reason why not all measured cases were presented in this paper since it was found that the Schlieren images were governed by the flame shape overall.

The evolution of the velocity field is shown in Fig. 13. The line-of-sight measurement is apparent for Case 1 since not only the stems of the V is visible, but the entire conical reaction front is captured by PIVlab – regardless that the middle region is less visible in the instantaneous images. This also applies to Fig. 13b, showing Case 3v. The 16 ms total time step with eight equidistant images equals 62.5 Hz. A frequency peak around 440 Hz is typical V-shaped flames [53,54], equivalent to a 2.3 ms time step; however, the periodic behavior was only found at 62.5 Hz.

The significantly increased velocity of NG compared to D at identical φ and thermal power is attributed to the concentrated reaction zone and hence the concentrated density gradients since the bulk flow velocities are similar. Even though D should feature a discrete V, combustion is present in a larger volume due to the less homogeneous fuel-air mixture, as shown previously in Fig. 10. Nevertheless, the periodic fluctuation near 62.5 Hz is also apparent here. The homogeneous NG-air mixture leads to complete combustion earlier; therefore, the local velocity field is random above the V, even though it is known that the flue gas leaves

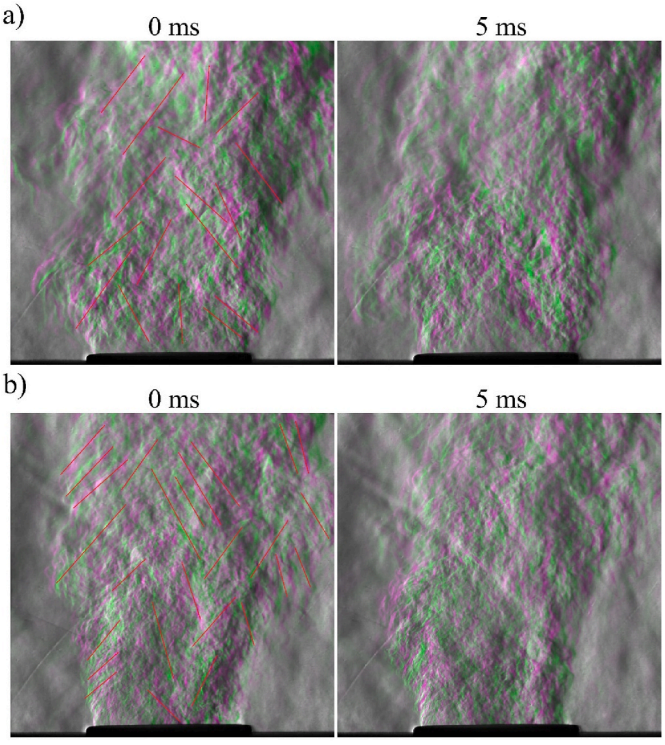

Fig. 12. False-color images of distributed flames at $\varphi = 0.67$. a) Case 7 ($p_g = 0.45$ bar) b) Case 9 ($p_g = 0.9$ bar). Red lines on the 0 ms images show some fishbone tile-shaped coherent structures.

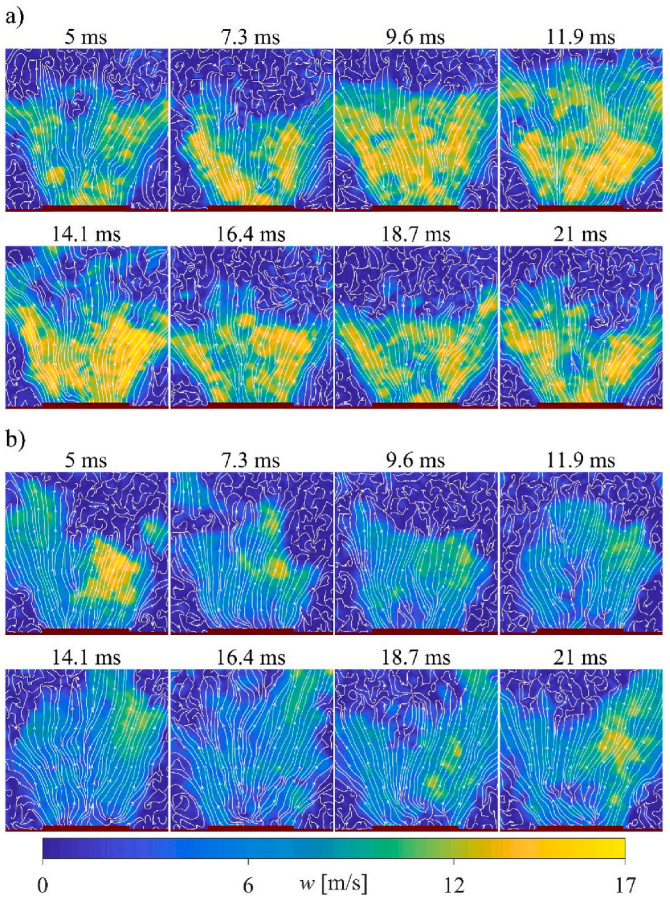

Fig. 13. Temporal evolution of the velocity field of V-shaped flames. a) Case 1 (NG) b) Case 3v (D).

straight downstream. This is present in the case of D, but only a few small burning packets reveal the real flow field.

Fig. 14 shows the velocity field of two distributed combustion cases using a 0.6 ms time step. Since no characteristic peak was found in the Schlieren images, this choice was made to show the temporal evolution of the igniting small mixture packets. The coherent structures here are similar to the findings of the false-color analysis, i.e., qualitatively following fishbone tile-shaped patterns. The dominantly vertical and oblique distributed structures are critical for a stable flame. The small flashing packets, meaning areas with $w > 10$ m/s, are only present for a small period, and their numbers are similar, meaning continuous ignition and burnout across the combustion chamber. Since the bulk flow velocity at $\varphi = 0.76$ is lower, ignition occurs closer to the burner lip in Fig. 14b. Also, the fast packets are relatively concentrated due to the lower bulk flow velocity, and they ignite the neighboring packets easier.

The temporal evolution of the velocity field of two further distributed combustion cases with 0.6 ms time step is shown in Fig. 15, featuring similar bulk flow velocity with a difference in p_g. The fishbone tile-shaped coherent structures are apparent here, similar to the false-color image analysis in Fig. 12. The lower atomizing pressure of Case 7 shows a more homogeneous velocity field with more uniformly distributed high-velocity mixture packets, shown by areas with $w > 10$ m/s. The ignition and the accompanying high-velocity packets appear earlier in Fig. 15b since elevated p_g leads to a more homogeneous mixture and smaller packet sizes, already presented in Fig. 12.

4. Conclusions

The possibility of distributed combustion outside of the MILD regime was demonstrated earlier with the accompanying ultra-low emissions

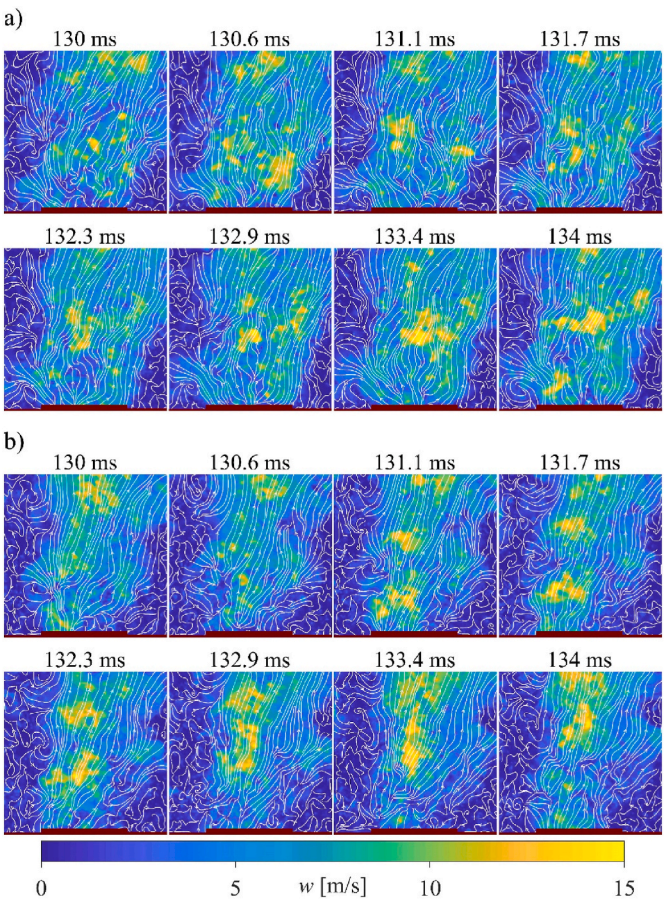

Fig. 14. Temporal evolution of the velocity field of distributed combustion at $p_g = 0.75$ bar. a) Case 4 ($\varphi = 0.57$) and b) Case 6 ($\varphi = 0.76$).

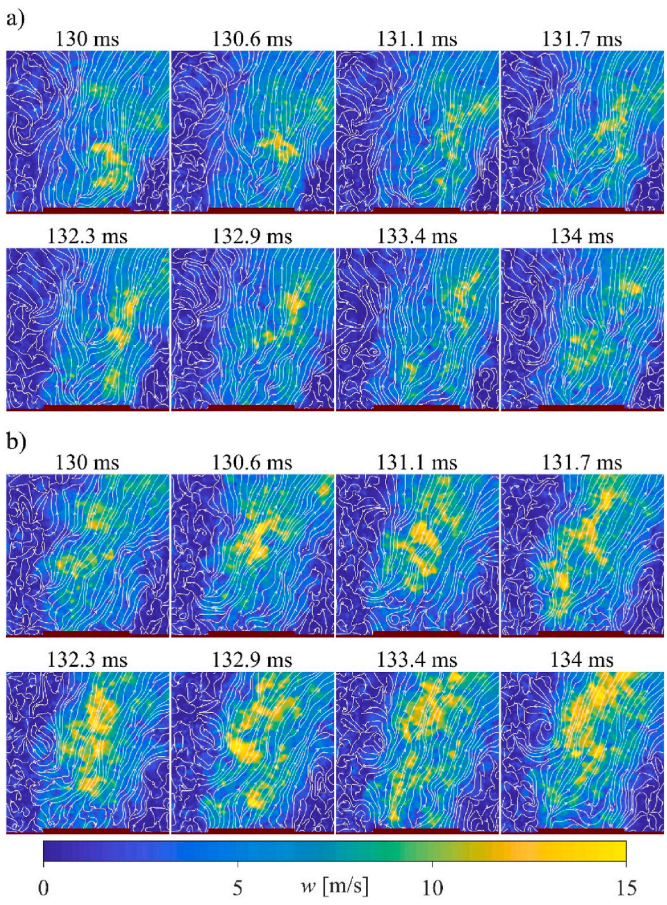

Fig. 15. Temporal evolution of the velocity field of distributed combustion at $\varphi = 0.67$. a) Case 7 ($p_g = 0.45$ bar) b) Case 9 ($p_g = 0.9$ bar).

[14]. The goal of this paper was to analyze the flame structure directly with the Schlieren technique that delivers line-of-sight qualitative information on density gradients. V-shaped and straight flames were also evaluated for reference, utilizing diesel fuel and natural gas. The following conclusions were derived based on the direct analysis of the images and the calculated velocity field by PIVlab.

1. It was hypothesized in Ref. [14] that distributed combustion is achieved by cooling the vicinity of the fuel jet and confining the ignition well downstream of the burner inside the combustion chamber. The Schlieren images confirmed this statement.
2. Both mean and RMS intensity images of 2000 frames show that the discharging cold fuel-air mixture features a notable density gradient at the burner lip, while the random fluctuations result in blurry characteristics when the mixture is igniting. Therefore, distributed combustion is free from a characteristic reaction zone, typical in V-shaped flames of swirl burners or straight flames.
3. The flame shape principally governs mean and RMS characteristics; the effect of the equivalence ratio and atomizing pressure were qualitatively low. However, all mean and RMS velocity and shear rates increased with atomizing pressure.
4. False-colored images and the temporal evolution of the velocity field revealed that the excellent blowout stability of distributed combustion results from the absence of dominant flow structures. Ignition occurs at numerous points, featuring quickly decaying burning packets. Numerous smaller random and larger coherent structures, either a fishbone tile or vertical-shaped, ensure seamless continuous combustion.

The results contributed to a better understanding of distributed combustion outside the MILD regime, concluding that the flame shape governs the heat release patterns. The findings can be used to develop advanced combustion systems for ultra-low emission boilers, furnaces, and gas turbines. This is justified by the more than 50% NO_X reduction and the freedom from thermoacoustic oscillations, compared to V-shaped flames of swirl burners, demonstrated in previous works. The current results quantitatively show the delayed mixture ignition and the fine structure of the distributed flame, leading to a better understanding of the heat liberation process to help combustion chamber design around the MTC combustion concept. As for future work, developing next-generation burners for, e.g., hydrogen and ammonia in the distributed combustion regime would be beneficial. The Schlieren technique is an excellent tool for evaluating and comparing their performance.

Credit author statement

Viktor Józsa: Conceptualization, Methodology, Validation, Investigation, Resources, Writing - Original Draft, Writing - Review & Editing, Visualization, Supervision, Project administration, Funding acquisition, **Milan Malý:** Conceptualization, Methodology, Validation, Investigation, Resources, Writing - Original Draft, Project administration, Funding acquisition, **Dániel Füzesi:** Methodology, Software, Formal analysis, Investigation, Data Curation, Writing - Original Draft, Visualization, **Erika Rácz:** Methodology, Software, Validation, Formal analysis, Investigation, Data Curation, Visualization, **Réka Anna Kardos:** Validation, Investigation, **Jan Jedelský:** Resources, Writing - Review & Editing, Supervision, Project administration, Funding acquisition.

Funding

The research reported in this paper was supported by the János Bolyai Research Scholarship of the Hungarian Academy of Sciences, National Research, Development and Innovation Fund of Hungary, project N⁰.s OTKA-FK 124704, 137758, ÚNKP-22-5-BME-304, ÚNKP-22-3-II-BME-100, ÚNKP-22-2-III-BME-79, and BME-NVA-02 by the Ministry of Innovation and Technology of Hungary from the National Research, Development and Innovation Fund, financed under the TKP2021 funding scheme. The support of the project "Computer Simulations for Effective Low-Emission Energy Engineering" was funded as project No. CZ.02.1.01/0.0/0.0/16_026/0008392 by Operational Programme Research, Development and Education, Priority axis 1: Strengthening capacity for high-quality research.

Declaration of competing interest

The authors declare the following financial interests/personal relationships which may be considered as potential competing interests: Viktor Jozsa reports financial support was provided by National Research Development and Innovation Office and Hungarian Academy of Sciences. Daniel Fuzesi reports financial support was provided by National Research Development and Innovation Office. Erika Racz reports financial support was provided by National Research Development and Innovation Office. Reka Anna Kardos reports financial support was provided by National Research Development and Innovation Office. Milan Maly reports financial support was provided by Ministry of Education Youth and Sports. Jan Jedelsky reports financial support was provided by Ministry of Education Youth and Sports.

Data availability

Data will be made available on request.

Appendix A. Supplementary data

Supplementary data to this article can be found online at https://doi.org/10.1016/j.energy.2023.127230.

References

[1] Kim EH, Park YG, Roh JH. Competitiveness of open-cycle gas turbine and its potential in the future Korean electricity market with high renewable energy mix. Energy Pol 2019;129:1056–69. https://doi.org/10.1016/j.enpol.2019.03.014.
[2] Ding X, Sun W, Harrison GP, Lv X, Weng Y. Multi-objective optimization for an integrated renewable, power-to-gas and solid oxide fuel cell/gas turbine hybrid system in microgrid. Energy 2020;213:118804. https://doi.org/10.1016/j.energy.2020.118804.
[3] European Commission. Sustainable aviation fuels – ReFuelEU aviation. 2021. https://ec.europa.eu/info/law/better-regulation/have-your-say/initiatives/12303-Sustainable-aviation-fuels-ReFuelEU-Aviation_en. [Accessed 13 October 2021]. accessed.
[4] Lefebvre AH, Ballal DR. Gas turbine combustion. third. Boca Raton: CRC Press; 2010. https://doi.org/10.1201/9781420086058.
[5] Perpignan AAV, Gangoli Rao A, Roekaerts DJEM. Flameless combustion and its potential towards gas turbines. Prog Energy Combust Sci 2018;69:28–62. https://doi.org/10.1016/j.pecs.2018.06.002.
[6] Huang Y, Yang V. Dynamics and stability of lean-premixed swirl-stabilized combustion. Prog Energy Combust Sci 2009;35:293–364. https://doi.org/10.1016/j.pecs.2009.01.002.
[7] Bowman C. Control of combustion-generated nitrogen oxide emissions: technology driven by regulation. Symp Combust 1992:859–78.
[8] Ballester J, García-Armingol T. Diagnostic techniques for the monitoring and control of practical flames. Prog Energy Combust Sci 2010;36:375–411. https://doi.org/10.1016/j.pecs.2009.11.005.
[9] Rahman ZU, Wang X, Zhang J, Yang Z, Dai G, Verma P, et al. Nitrogen evolution , NOx formation and reduction in pressurized oxy coal combustion. Renew Sustain Energy Rev 2022;157:112020. https://doi.org/10.1016/j.rser.2021.112020.
[10] Zheng S, Qian Y, Wang X, Vujanovic M, Zhang Y, Rahman ZU, et al. Experimental investigation of the NO x formation and control during the self-sustaining incineration process of N-containing VOCs (DIMETHYLFORMAMIDE). Fuel 2022;315:123149. https://doi.org/10.1016/j.fuel.2022.123149.
[11] Liu Y, Sun X, Sethi V, Nalianda D, Li YG, Wang L. Review of modern low emissions combustion technologies for aero gas turbine engines. Prog Aero Sci 2017;94:12–45. https://doi.org/10.1016/j.paerosci.2017.08.001.
[12] Roy R, Gupta AK. Flame structure and emission signature in distributed combustion. Fuel 2020;262:116460. https://doi.org/10.1016/j.fuel.2019.116460.
[13] Xing F, Kumar A, Huang Y, Chan S, Ruan C, Gu S, et al. Flameless combustion with liquid fuel: a review focusing on fundamentals and gas turbine application. Appl Energy 2017;193:28–51. https://doi.org/10.1016/j.apenergy.2017.02.010.
[14] Józsa V. Mixture temperature-controlled combustion: a revolutionary concept for ultra-low NOX emission. Fuel 2021;291:120200. https://doi.org/10.1016/j.fuel.2021.120200.
[15] Sharma S, Chowdhury A, Kumar S. A novel air injection scheme to achieve MILD combustion in a can-type gas turbine combustor. Energy 2020;194:116819. https://doi.org/10.1016/j.energy.2019.116819.
[16] Reddy VM, Trivedi D, Sawant D, Kumar S. Investigations on emission characteristics of liquid fuels in a swirl combustor. Combust Sci Technol 2015;187:469–88. https://doi.org/10.1080/00102202.2014.956098.
[17] Füzesi D, Maly M, Jedelský J, Józsa V, Malý M, Jedelský J, et al. Numerical modeling of distributed combustion without air dilution in a novel ultra-low emission turbulent swirl burner. Phys Fluids 2022:043311. https://doi.org/10.1063/5.0085058.
[18] Józsa V, Hidegh GT, Csemány D, Kardos RA, Chong CT. Dynamics and emission of nearly flameless combustion of waste cooking oil biodiesel in an ultra-low emission non-MILD swirl burner. Fuel 2022;319:123743. https://doi.org/10.1016/j.fuel.2022.123743.
[19] Guvernyuk S, Simonenko M, Zubkov A. Experimental study of supersonic flow around an axisymmetric annular cavity at angles of attack. Acta Astronaut 2021;180:693–700. https://doi.org/10.1016/j.actaastro.2021.01.013.
[20] Cammi G, Spinelli A, Cozzi F, Guardone A. Automatic detection of oblique shocks and simple waves in schlieren images of two-dimensional supersonic steady flows. Meas J Int Meas Confed 2021;168:108260. https://doi.org/10.1016/j.measurement.2020.108260.
[21] Lai Y, Wang X, Rockett TBO, Willmott JR, Zhang Y. Investigation into wind effects on fire spread on inclined wooden rods by multi-spectrum and schlieren imaging. Fire Saf J 2022;127:103513. https://doi.org/10.1016/j.firesaf.2021.103513.
[22] Cao Y, Dahari M, Tlili I, Raise A. Investigation on the laminar flame speed of CH4/CO2/air mixture at atmospheric and high pressures using Schlieren photography. Int J Hydrogen Energy 2020;45:31151–61. https://doi.org/10.1016/j.ijhydene.2020.08.061.
[23] Ibarreta AF, Sung CJ, Hirasawa T, Wang H. Burning velocity measurements of microgravity spherical sooting premixed flames using rainbow SCHLIEREN deflectometry. Combust Flame 2005;140:93–102. https://doi.org/10.1016/j.combustflame.2004.10.007.
[24] Ge Y, Li S, Wei X. Combustion states distinction of the methane/oxygen laminar co-flow diffusion flame at high pressure. Fuel 2019;243:221–9. https://doi.org/10.1016/j.fuel.2019.01.113.
[25] Grauer SJ, Unterberger A, Rittler A, Daun KJ, Kempf AM, Mohri K. Instantaneous 3D flame imaging by background-oriented schlieren tomography. Combust Flame 2018;196:284–99. https://doi.org/10.1016/j.combustflame.2018.06.022.
[26] Yen SC, Ye CE, San KC. Effects of starlike control discs on flow structures and combustion capability. Energy 2021;225:120276. https://doi.org/10.1016/j.energy.2021.120276.
[27] Hariharan V, Mishra DP. Entrainment studies in inverse jet flame port burner. Combust Flame 2020;216:338–53. https://doi.org/10.1016/j.combustflame.2020.02.023.
[28] Xiao H, Houim RW, Oran ES. Formation and evolution of distorted tulip flames. Combust Flame 2015;162:4084–101. https://doi.org/10.1016/j.combustflame.2015.08.020.
[29] Owaki T, Umemura A. Premixed swirl combustion modes emerging for a burner tube with converging entrance. Proc Combust Inst 2007;31 I:1067–74. https://doi.org/10.1016/j.proci.2006.08.072.
[30] Wang Q, Wang J, Mei X, Sun Y, Sun M, Zhu J, et al. Imaging-based harmonic frequency analysis of a bluff-body premixed flame under acoustic excitations. Aero Sci Technol 2022;120:107254. https://doi.org/10.1016/j.ast.2021.107254.
[31] Caux-Brisebois V, Steinberg AM, Arndt CM, Meier W. Thermo-acoustic velocity coupling in a swirl stabilized gas turbine model combustor. Combust Flame 2014;161:3166–80. https://doi.org/10.1016/j.combustflame.2014.05.020.
[32] Fugger CA, Hsu PS, Jiang N, Yi T, Slipchenko MN, Felver JJ, et al. 10-kHz simultaneous dual-plane stereo-PIV and OH-PLIF imaging. Appl Phys B Laser Opt 2020;126:1–9. https://doi.org/10.1007/s00340-020-07522-4.
[33] Thielicke W, Sonntag R. Particle image velocimetry for MATLAB: accuracy and enhanced algorithms in PIVlab. J Open Res Software 2021;9:1–14. https://doi.org/10.5334/JORS.334.
[34] Stopper U, Meier W, Sadanandan R, Stöhr M, Aigner M, Bulat G. Experimental study of industrial gas turbine flames including quantification of pressure influence on flow field, fuel/air premixing and flame shape. Combust Flame 2013;160:2103–18. https://doi.org/10.1016/j.combustflame.2013.04.005.
[35] Pastor JV, Payri R, Garcia-Oliver JM, Nerva JG. Schlieren measurements of the ECN-spray a penetration under inert and reacting conditions. SAE Tech Pap 2012. https://doi.org/10.4271/2012-01-0456.
[36] Tigáz-DSO Földgázelosztó Kft. Composition of natural gas (in Hungarian). 2021.
[37] Beér JM, Chigier NA. Combustion aerodynamics. London: Robert E. Krieger Publishing Company, Inc.; 1972.
[38] Wünning JA, Wünning JG. Flameless oxidation to reduce thermal NO-formation. Prog Energy Combust Sci 1997;23:81–94. https://doi.org/10.1016/s0360-1285(97)00006-3.

[39] MathWorks. MATLAB, release. 2021. 2021.
[40] Stamhuis EJ. Basics and principles of particle image velocimetry (PIV) for mapping biogenic and biologically relevant flows. Aquat Ecol 2006;40:463–79. https://doi.org/10.1007/s10452-005-6567-z.
[41] Sciacchitano A, Wieneke B, Scarano F. PIV uncertainty quantification by image matching. Meas Sci Technol 2013;24. https://doi.org/10.1088/0957-0233/24/4/045302.
[42] Liu H, Shui C, Cai W. Time-resolved three-dimensional imaging of flame refractive index via endoscopic background-oriented Schlieren tomography using one single camera. Aero Sci Technol 2020;97:105621. https://doi.org/10.1016/j.ast.2019.105621.
[43] Panoutsos C, Hardalupas Y, Taylor A. Numerical evaluation of equivalence ratio measurement using OH* and CH* chemiluminescence in premixed and non-premixed methane–air flames. Combust Flame 2009;156:273–91. https://doi.org/10.1016/j.combustflame.2008.11.008.
[44] Shanbhogue SJ, Sanusi YS, Taamallah S, Habib MA, Mokheimer EMA. Flame macrostructures , combustion instability and extinction strain. Combust Flame 2015:1–14. https://doi.org/10.1016/j.combustflame.2015.10.026.
[45] Marragou S, Magnes H, Poinsot T, Selle L, Schuller T. Stabilization regimes and pollutant emissions from a dual fuel CH4/H2 and dual swirl low NOx burner. Int J Hydrogen Energy 2022;47:19275. https://doi.org/10.1016/j.ijhydene.2022.04.033. –88.
[46] Belal BY, Li G, Zhang Z, El-Batsh HM, Moneib HA, Attia AMA. The effect of swirl burner design configuration on combustion and emission characteristics of lean pre-vaporized premixed flames. Energy 2021;228:120622. https://doi.org/10.1016/j.energy.2021.120622.
[47] Huang M, Li R, Xu J, Cheng S, Deng H, Rong Z, et al. Effect of equivalence ratio and staging ratio on the methane MILD combustion in dual-stage combustor. Fuel 2022;307:121903. https://doi.org/10.1016/j.fuel.2021.121903.
[48] Masri AR. Challenges for turbulent combustion. Proc Combust Inst 2021;38:121–55. https://doi.org/10.1016/j.proci.2020.07.144.
[49] Sankaran R, Im HG, Hawkes ER, Chen JH. The effects of non-uniform temperature distribution on the ignition of a lean homogeneous hydrogen-air mixture. Proc Combust Inst 2005;30:875–82. https://doi.org/10.1016/j.proci.2004.08.176.
[50] Ahmed MMA, Birouk M. Effect of fuel nozzle geometry on swirling partially premixed methane flames. J Eng Gas Turbines Power 2020;142:1–16. https://doi.org/10.1115/1.4045477.
[51] Mikelsons K, Wang M. Global clear sky near-surface imagery from multiple satellite daily imagery time series. ISPRS J Photogrammetry Remote Sens 2021;180:238–54. https://doi.org/10.1016/j.isprsjprs.2021.08.013.
[52] Al-Abdeli YM, Masri AR. Review of laboratory swirl burners and experiments for model validation. Exp Therm Fluid Sci 2015;69:178–96. https://doi.org/10.1016/j.expthermflusci.2015.07.023.
[53] Runyon J, Marsh R, Bowen P, Pugh D, Giles A, Morris S. Lean methane flame stability in a premixed generic swirl burner: isothermal flow and atmospheric combustion characterization. Exp Therm Fluid Sci 2018;92:125–40. https://doi.org/10.1016/j.expthermflusci.2017.11.019.
[54] Durox D, Moeck JP, Bourgouin JF, Morenton P, Viallon M, Schuller T, et al. Flame dynamics of a variable swirl number system and instability control. Combust Flame 2013;160:1729–42. https://doi.org/10.1016/j.combustflame.2013.03.004.